Theory of quasiparticle scattering in a two-dimensional system of helical Dirac fermions: Surface band structure of a three-dimensional topological insulator

Xiaoting Zhou, Chen Fang, Wei-Feng Tsai, and JiangPing Hu
Department of Physics, Purdue University, West Lafayette, Indiana 47907, USA
(Received 8 October 2009; revised manuscript received 24 November 2009; published 18 December 2009)

We study the quasiparticle interference (QPI) patterns caused by scattering off nonmagnetic, magnetic point impurities, and edge impurities, separately, in a two-dimensional helical liquid, which describes the surface states of a topological insulator. The unique features associated with hexagonal warping effects are identified in the QPI patterns of charge density with nonmagnetic impurities and spin density with magnetic impurities. The symmetry properties of the QPI patterns can be used to determine the symmetry of microscopic models. The Friedel oscillation is calculated for edge impurities and the decay of the oscillation is not universal, strongly depending on Fermi energy. Some discrepancies between our theoretical results and current experimental observations are discussed.

DOI: 10.1103/PhysRevB.80.245317 PACS number(s): 73.20.−r, 73.50.Bk, 73.43.Cd

I. INTRODUCTION

Several recent theoretical[1–3] and experimental[4–9] works have focused on a new quantum state of matter, *topological insulators* in three dimensions (3D), which exhibit bulk insulating gaps (mainly of spin-orbit origin) while possess *time-reversal symmetry* protected gapless surface states. One of intriguing properties in this new quantum state comes from those "protected" surface states, which provide a lab-realizable condensed-matter analog of two-dimensional (2D), massless Dirac theory with "odd" number of species (Dirac cones), in the surface Brillouin zone (SBZ).[1,10] The charge carriers on the surfaces here, the so-called (spin) *helical* Dirac fermions,[6,11] behave like relativistic particles with a spin locked to its momentum leading to the breakdown of the spin-SU(2) rotational symmetry. This feature is sharply in contrast to graphene, where the system not only possesses an even number of Dirac cones in its spectrum but the role of the "locked" spin is also replaced by a pseudospin (sublattice symmetry) and hence each Dirac cone still has twofold spin degeneracy.[12]

As a useful surface probe, recent angle-resolved photoemission spectroscopy (ARPES) experiments successfully demonstrated the surface band structures with odd number of Dirac cones[4,7] as well as the corresponding spin-helical structures near a Dirac point.[5,6,8] Although the confirmed nature of the bands by ARPES suggests the quantum state to be topologically insulating, the quest for new quantum phenomena uniquely associated with such topology-protected surface states remains urgent and necessary. The usual way in solid-state physics to explore the nontrivial electronic properties of helical Dirac fermion systems would be the transport measurement on the surface of a topological insulator.[10] However, such a measurement may not be practically straightforward since (i) tuning the system to the topological transport regime where the charge density vanishes is tricky and (ii) the presence of the *n*-type doping from vacancy (or antisite defects) as well as the fact that the surface states surround the sample make the results difficult to be distinguished from the bulk and surface contributions.[7,13]

Alternatively, the quasiparticle interference (QPI) caused by scattering-off impurities on a surface can provide a way of revealing the topological nature of the surface states.[14–17] The concept of QPI is elementary in quantum mechanics. For instance, due to impurity (elastic) scattering, the interference between the incoming and outgoing waves with momenta $\mathbf{k}_i$ and $\mathbf{k}_f$, respectively, can give rise to an amplitude modulation in the local density of states (LDOS) at wave vector $\mathbf{q}=\mathbf{k}_f-\mathbf{k}_i$. Such kind of interference pattern can be observed in Fourier-transform (FT) scanning-tunneling spectroscopy nowadays and it has been proved useful in determining the pairing nature of high-T_c cuprates.[18] By measuring the QPI patterns and analyzing them through a convolution of ARPES data together with a spin-dependent scattering-matrix element, Roushan *et al.*[14] were able to demonstrate the absence of backscattering in the topological surface states of $Bi_{1-x}Sb_{x'}$, a key property of helical liquid.

Most recently, based on symmetry analysis, a new hexagonal warping term, which is absent in $Bi_{1-x}Sb_{x'}$, is suggested by Liang Fu[19] to explain the evolution of the Fermi surface of the effective 2D helical Dirac model describing the surface band structure of a family of 3D topological insulators, Bi_2X_3 (X=Se or Te). As measured in ARPES experiments, the shape of the Fermi surface (FS) evolves gradually from a hexagram, a hexagon, to a circle of shrinking volume, and finally meets at the Dirac point when lowering the Fermi energy. The new term leads to strong density variation around Fermi surface and also modifies the spin-helical configuration. As a result, the existence of the new term can strongly modify the QPI. In other words, the QPI can provide a direct evidence to justify the model.

In this paper we systematically investigate the interference effects of a point-impurity and an edge-impurity scattering, respectively, on the LDOS in a 2D helical Dirac fermion system. We use T-matrix approach to calculate QPI spectra at a few representative energies, for emphasizing the effects of the hexagonal warping term, in the presence of a nonmagnetic/magnetic impurity. We also investigate an edge impurity by using a method generalized from one-dimensional (1D) scattering problems with a potential barrier. Several profound features are found in this study. In a nutshell, we observe: (i) the backward scattering by nonmagnetic point impurities is topologically suppressed, just as

what has been shown in Ref. 14 with a simpler empirical analysis and the dominant interference pattern becomes that of spatial period $2\pi/|\mathbf{q}_{35}|$ when going away from the Dirac regime (see Fig. 4 for the definition of $\mathbf{q}_{35}$); (ii) In the presence of magnetic impurity, the QPI of charge density is very weak while that of spin density becomes strong. Near the Dirac regime, spin moments of fermions are flipped when scattering wave vector crosses over $|\mathbf{q}|=2|\mathbf{k}_F|$ as demonstrated in the (z-component) spin LDOS [see Fig. 8(b)]; (iii) the mirror symmetries of the spin LDOS in the presence of in-plane magnetic impurity with spin polarization fixed along x and y directions can be used to determine the symmetry of microscopic models and to verify the presence or absence of the warping term; (iv) in the case of 1D edge impurities, the Friedel oscillation has no universal decaying function. Depending on Fermi-surface energy, we show that the oscillation decays as $1/\sqrt{|x|}$ if the FS shape is dominated by the warping term and as $|x|^{-3/2}$ if the warping term is negligible. These special quantum phenomena, sharply in contrast to conventional metals, are mainly associated with the 2D helical liquid.

II. THE MODEL AND *T*-MATRIX FORMALISM

We now briefly introduce our used formalism below. The explicit model we study here is written as

$$H(\mathbf{k}) = v(k_x\sigma_y - k_y\sigma_x) + \frac{k^2}{2m^*} + \frac{\lambda}{2}(k_+^3 + k_-^3)\sigma_z, \qquad (1)$$

where $k_\pm \equiv k_y \pm ik_x$. v and λ denote Fermi velocity and hexagonal warping parameter, respectively. The Pauli matrices, σ_i, act on spin space of fermionic quasiparticles. The form of $H(\mathbf{k})$ is suitable for describing the [111] surface band structure near Γ point in SBZ of a 3D topological insulator Bi_2X_3 and is fixed under general symmetry considerations, namely, time-reversal and C_{3v} symmetries.[19] Notice that we have chosen x direction to be along ΓM in SBZ. The k-linear term, $H_0=v(k_x\sigma_y-k_y\sigma_x)$, describes an isotropic 2D helical Dirac fermions and the k-square term causes particle-hole asymmetry. More importantly, the k-cube warping term, $H_w = \frac{\lambda}{2}(k_+^3+k_-^3)\sigma_z$, leads to hexagonal distortion of the Fermi surface. The resulting two energy bands now touch at the Dirac point (i.e., Γ point in SBZ) with dispersion relation

$$\epsilon_\pm(\mathbf{k}) = \frac{k^2}{2m^*} \pm \sqrt{v^2k^2 + \frac{\lambda^2}{4}(k_+^3 + k_-^3)^2}. \qquad (2)$$

Defining the characteristic length scale $b \equiv \sqrt{\lambda/v}$ and energy $E^* \equiv v/b$ introduced by the hexagonal warping parameter, we draw the contours of constant energy (CCE) in momentum space in units of $1/b$ and single-particle DOS of $H(\mathbf{k})$, respectively, in Figs. 1 and 2.

In the numerical evaluation, we have taken $b \equiv 1$, $v=0.25$, and $\lambda=0.25$ such that the Fermi surface in 0.67% Sn-doped Bi_2Te_3 can be qualitatively reproduced, where the measured $v=2.55$ eV Å and $E_F=1.2E^* \approx 0.3$ eV. Unless otherwise stated, we will assume particle-hole symmetry, i.e., $m^* \to \infty$. As shown in Figs. 1 and 2, when $\omega \ll 0.2$ the DOS is almost linear in ω with more circular FS while when $\omega \gg 0.2$ the DOS behaves like $\omega^{-1/3}$ with hexagramlike FS.

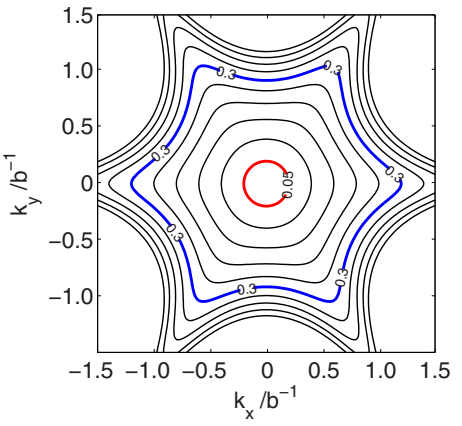

FIG. 1. (Color online) Contours of constant energy and the evolution of FS.

In addition to the CCE, we also present the spin-resolved FS with two representative energies used throughout this paper, $E_D=0.05$ eV ($0.2E^*$) and $E_W=0.3$ eV ($1.2E^*$) in Fig. 3. They clearly demonstrate the "spin-helical" nature of the 2D fermions, which is indeed essential when analyzing the QPI spectra later. In particular, as $\omega=E_W$, nonvanishing spin moments along z direction (out of surface plane) are present mainly due to σ_z in the warping term, which is directly proportional to electron's spin. Notice that the spin moment must be in-plane along ΓM (i.e., at each sharp vertex of the FS), which is a consequence of the odd parity of σ_z under the mirror operation $y \to -y$.

Next, we consider the quasiparticle scattering problem within the T-matrix approach.[20] For a general N-impurity problem, the impurity-induced electronic Green's function is given by

$$\delta G(\mathbf{r},\mathbf{r}',\omega) = \sum_{i,j=1}^{N} G_0(\mathbf{r},\mathbf{r}_i,\omega)T(\mathbf{r}_i,\mathbf{r}_j,\omega)G_0(\mathbf{r}_j,\mathbf{r}',\omega), \quad (3)$$

where the T matrix obeys the Bethe-Salpeter equation

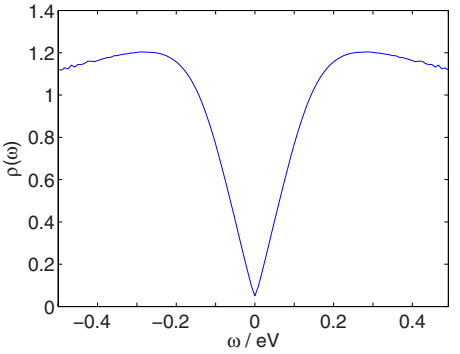

FIG. 2. (Color online) Density of states based on the model in Eq. (1).

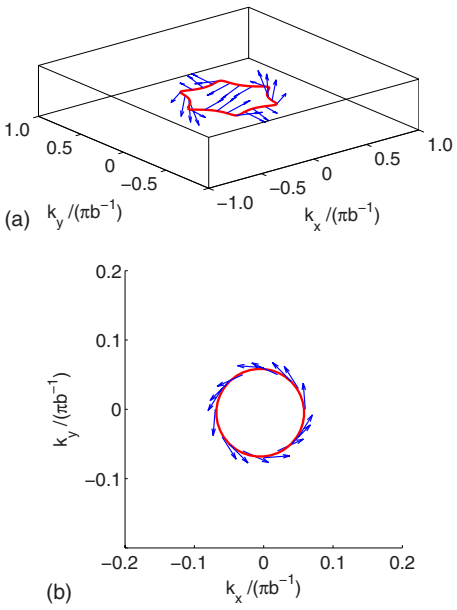

FIG. 3. (Color online) Spin textures around the Fermi surface at (a) $\omega=0.3$ eV and (b) $\omega=0.05$ eV).

$$T(\mathbf{r}_i,\mathbf{r}_j,\omega) = V_{\mathbf{r}_i}\delta_{\mathbf{r}_i,\mathbf{r}_j} + V_{\mathbf{r}_i}\sum_{k=1}^{N} G_0(\mathbf{r}_i,\mathbf{r}_k,\omega)T(\mathbf{r}_k,\mathbf{r}_j,\omega) \quad (4)$$

and the Green's function (in momentum space) of the clean system is

$$G_0(\mathbf{k},\omega) = [\omega + i\eta - H(\mathbf{k})]^{-1}. \quad (5)$$

In the case of a single-point nonmagnetic (magnetic) impurity located at the origin, the scattering potential is simply $V_{\mathbf{r}}=\delta_{\mathbf{r},0}V_{NI}\sigma_0$ ($\delta_{\mathbf{r},0}V_{MI}\vec{\sigma}$), where σ_0 is a 2×2 identity matrix. Taking the advantages of the translational symmetry of the clean system and momentum independence of the scattering potential (for instance, $V_{\mathbf{k},\mathbf{k}'}=V_{NI}\sigma_0/N\equiv\hat{V}$ in the nonmagnetic case), one can simplify the formula as

$$T(\omega) = \left[1 - \hat{V}\int_{\epsilon_+(\mathbf{k})<\Lambda}\frac{d^2k}{(2\pi)^2}G_0(\mathbf{k},\omega)\right]^{-1}\hat{V} \quad (6)$$

and hence around the impurity, spatial oscillations of the local density of states are induced. To see the interference effects due to impurity scattering, it is more convenient to compute the Fourier-transformed (induced) local density of states (FT-LDOS)

$$\int d^2r e^{i\mathbf{q}\cdot\mathbf{r}}\delta\rho(\mathbf{r},\omega) \sim \delta\rho(\mathbf{q},\omega) = \frac{i}{2\pi}\int_{\epsilon_+(\mathbf{k})<\Lambda}\frac{d^2k}{(2\pi)^2}g(\mathbf{k},\mathbf{q},\omega), \quad (7)$$

where $g(\mathbf{k},\mathbf{q},\omega)=\Sigma_{i=1}^{2}[\delta G_{ii}(\mathbf{k},\mathbf{k}+\mathbf{q},\omega)-\delta G_{ii}^{*}(\mathbf{k}+\mathbf{q},\mathbf{k},\omega)]$. In general, $\rho(\mathbf{q},\omega)$ is a complex number. If we separately define the symmetric and antisymmetric parts of the LDOS as $\rho^S(x,y,\omega)=[\rho(x,y,\omega)+\rho(-x,-y,\omega)]/2$ and $\rho^A(x,y,\omega)=[\rho(x,y,\omega)-\rho(-x,-y,\omega)]/2$, the real and imaginary parts of $\rho(\mathbf{q},\omega)$ simply describe the symmetric and antisymmetric parts of the LDOS, respectively. In the following discussion of the effects of nonmagnetic impurities since the real part is at least two orders of magnitude larger than the imaginary part, we focus on the former. In our calculation, we have introduced an energy cutoff $\Lambda=4E^*$ when integrating over momentum. Our main results do not sensitively depend on the chosen Λ as long as Λ is much greater than the impurity scattering strength. Moreover, the spin-resolved FT-LDOS can be obtained if we separate each component i when evaluating function $g(\mathbf{k},\mathbf{q},\omega)$, i.e., $i=1$ for spin up and $i=2$ for spin down.

In principle, for the case of an edge-impurity scattering, one can use Eqs. (3)–(5) to compute the LDOS from $\delta\rho(\mathbf{r},\omega)=-\mathrm{Im}\,\Sigma_i\delta G_{ii}(\mathbf{r},\mathbf{r},\omega)/\pi$ in a straightforward manner. However, it is more convenient, without loss of generality, to treat this scattering problem by using an analogy of the elementary scattering problem with a barrier potential in one dimension, which is directly based on the wave-function point of view. Our method is briefly sketched in Sec. III C.

III. NUMERICAL RESULTS

We compute the induced LDOS at selected ω, $\delta\rho(\mathbf{q},\omega)$, for the nonmagneic/magnetic impurity case, and, $\rho(q_x,\omega)$, for the edge-impurity case. Our numerical results are reported for a representative potential scattering strength, $V_{NI}=V_{MI}=V_0=0.05$ eV. The chosen imaginary part of the energy $\eta=10$ meV has been checked to be insensitive to the observed main features. Also, in our analysis a 400×400 momentum grid is used in $(-\pi,\pi)\times(-\pi,\pi)$ k space and 200 discrete points are displayed within $(-\pi,\pi)$ along each direction in q space. Note that the relevant range of SBZ in experiments would correspond to about 5.5 times larger than 2π.

A. Nonmagnetic point impurity

We first consider the interference patterns in a 2D helical liquid with a nonmagnetic point impurity. Starting with $\omega=E_W=0.3$ eV far away from the Dirac point ($\omega=0$), the shape of the FS is now like a hexagram. This is just the energy range where experiment may achieve without subtle chemical tuning near the surface of a 3D topological insulator. As we will see later, such energy range indeed provide a better chance to reveal the topological nature of the helical Fermion system. In Fig. 4, the spectral function, $\mathcal{A}(\mathbf{k},\omega)=-\frac{1}{\pi}\mathrm{Im}[\mathrm{Tr}\,G_0(\mathbf{k},\omega)]$ at $\omega=0.3$ eV, are plotted with scattering vectors on top, which are expected to associate with high-joint DOS on a constant-energy contour.

As shown in Fig. 5(a), the interference pattern includes six sharp peaks along ΓK outside a complicated, hexagon-shaped pattern centered at Γ and other six weaker peaks along ΓM slightly inside the hexagon. These two sets of peaks simply correspond to $(\pm\mathbf{q}_{13},\pm\mathbf{q}_{35},\pm\mathbf{q}_{51})$ and $(\pm\mathbf{q}_{12},\pm\mathbf{q}_{23},\pm\mathbf{q}_{34})$, respectively, as indicated in Fig. 4. However, the most prominent feature we observed here is that those expected peaks, which correspond to the $(\pm\mathbf{q}_{14},\pm\mathbf{q}_{25},\pm\mathbf{q}_{36})$, are entirely absent. This apparent puzzle can be understood by the absence of backscattering between two time-reversal-connected partners, as shown in Ref. 14. Suppose in our scattering problem, $|\mathbf{k},\uparrow\rangle$ is the in-

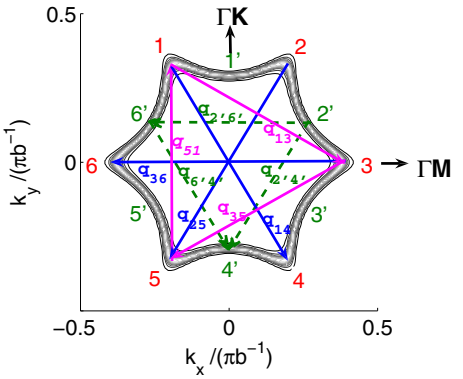

FIG. 4. (Color online) The spectral function $\mathcal{A}(\mathbf{k},\omega)$ at $\omega=0.3$ eV with three most possible scattering wave vectors. Note the wave vector is in units of πb^{-1} and brighter region corresponds to higher spectral weight.

coming state, while its time-reversal partner, $|-\mathbf{k},\downarrow\rangle \propto \mathcal{T}|\mathbf{k},\uparrow\rangle$, is the outgoing state. $\mathcal{T}$ is the time-reversal operator with the property $\mathcal{T}^2=-1$. For any time-reversal invariant and Hermitian operator $\hat{V}$ (such as our nonmagnetic scattering potential), we have

$$\begin{aligned}\langle -\mathbf{k},\downarrow|\hat{V}|\mathbf{k},\uparrow\rangle &= \langle \mathcal{T}(\mathbf{k},\uparrow)|\hat{V}(\mathbf{k},\uparrow)\rangle = \langle \mathcal{T}\hat{V}(\mathbf{k},\uparrow)|\mathcal{T}^2(\mathbf{k},\uparrow)\rangle \\ &= -\langle \mathbf{k},\uparrow|\mathcal{T}\hat{V}|\mathbf{k},\uparrow\rangle^* = -\langle \mathbf{k},\uparrow|\hat{V}\mathcal{T}|\mathbf{k},\uparrow\rangle^* \\ &= -\langle \mathbf{k},\uparrow|\hat{V}|-\mathbf{k},\downarrow\rangle^* = -\langle -\mathbf{k},\downarrow|\hat{V}^\dagger|\mathbf{k},\uparrow\rangle \\ &= -\langle -\mathbf{k},\downarrow|\hat{V}|\mathbf{k},\uparrow\rangle = 0. \end{aligned} \tag{8}$$

In other words, the backward scattering between time-reversal partners is not allowed. This naturally explains the absence of the interference peaks, corresponding to $\mathbf{q}_{36}$ (and of the same type). Such a behavior sharply distinguishes the 2D helical Fermion system from a conventional metal. In addition, it might be worth mentioning here that the angles of our observed interference peaks, $\mathbf{q}_{35}$, appear different from the experiment done by Zhang *et al.*,[15] where there exhibits six peaks along ΓM, instead of ΓK as displayed in Fig. 5(a). We would like to postpone this issue to the discussion section.

When further increasing the Fermi level, the vertices become sharper and the joint DOS at fixed $\mathbf{q}_{35}$, however, is suppressed. As a result, the six peaks seen in Fig. 5(a) diminish and the replaced feature turns out to be the other six peaks at fixed $\mathbf{q}'$, corresponding to the scattering vectors connecting between second neighbor of the convex parts of the FS (see Fig. 6), which were observed in recent experiments.[15] On the other hand, when the Fermi level gets closer to the Dirac point, for instance, $\omega=0.05$ eV, the interference pattern becomes almost isotropic with obvious stronger weight within a circular region, as shown in Fig. 5(b). The size of the region can be estimated to be a disk with twice longer radius of the corresponding circular FS of the system. This is basically consistent with our CCE picture (see Fig. 1), where no finite, specific $\mathbf{q}$ vectors can be picked out when ω approaches to the Dirac point.

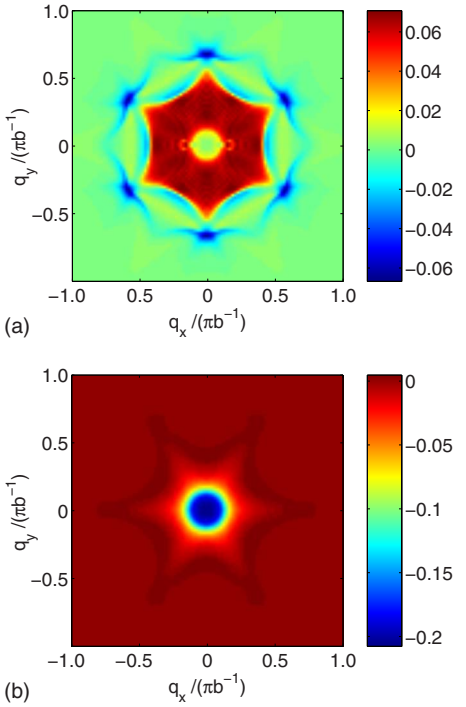

FIG. 5. (Color online) The real part of the Fourier transform of local density of states in the case of single nonmagnetic point impurity at (a) $\omega=0.3$ eV and (b) $\omega=0.05$ eV.

B. Classical magnetic point impurity

Next, we study the QPI induced by a time-reversal symmetry breaker, a magnetic impurity.[21] We focus on the effects of a classical magnetic impurity so that the Kondo physics is ignored. In the following, after describing general features of the QPI with a magnetic impurity, we will discuss the cases separately when the impurity moment is fixed along x, y, and z directions.

Different from nonmagnetic impurities, a weak magnetic impurity has very little effect on the charge density of the system, namely, instead of having $\delta\rho_\uparrow(\mathbf{q},\omega)=\delta\rho_\downarrow(\mathbf{q},\omega)$ as in the nonmagnetic impurity case, we have $\delta\rho_\uparrow(\mathbf{q},\omega) \approx -\delta\rho_\downarrow(\mathbf{q},\omega)$. This effect can be easily understood. Suppose we are considering an impurity moment along the

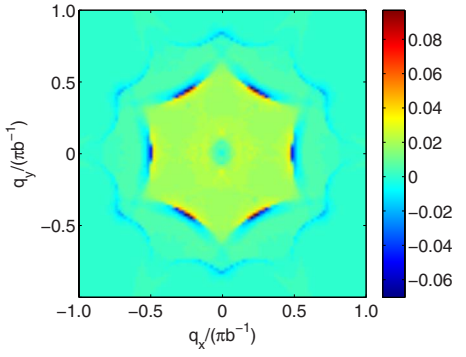

FIG. 6. (Color online) The real part of the Fourier transform of local density of states in the case of single nonmagnetic point impurity at $\omega=0.375$ eV.

z direction then the spin-up electrons and spin-down electrons see two scattering potentials of opposite signs. In the lowest order of perturbation theory, the scattering amplitude of the spin-up and spin-down electrons thus differ by a minus sign so that the total interference pattern of the charge density vanishes almost everywhere. The same argument no longer holds if higher orders of perturbation are included. For the model considered here, we can explicitly prove the above statement. Assuming $V \ll \omega$, the approximation $T(\omega) \approx \hat{V}$ becomes sufficiently accurate. In this case (impurity moment along z direction), we have

$$\begin{aligned}
\mathrm{Tr}[\delta G(\mathbf{q},\omega)] &\approx \int \frac{d^2k}{(2\pi)^2} \mathrm{Tr}[G_0(\mathbf{k},\omega)\hat{V}G_0(\mathbf{k}+\mathbf{q},\omega)] \\
&= V\int \frac{d^2k}{(2\pi)^2} \frac{\mathrm{Tr}\left[\left[\omega\sigma_0 - k_y\sigma_x + k_x\sigma_y + \frac{\lambda}{2}(k_+^3 + k_-^3)\sigma_z\right]\sigma_z\left\{\omega\sigma_0 - (k_y+q_y)\sigma_x + (k_x+q_x)\sigma_y + \frac{\lambda}{2}[(k+q)_+^3 + (k+q)_-^3]\sigma_z\right\}\right]}{[(\omega+i\eta)^2 - \epsilon_+^2(\mathbf{k})][(\omega+i\eta)^2 - \epsilon_+^2(\mathbf{k}+q)]} \\
&= V\int \frac{d^2k}{(2\pi)^2}\left\{2\frac{k_+^3 + k_-^3 + (k+q)_+^3 + (k+q)_-^3 + ik_y(k_x+q_x) - ik_x(k_y+q_y)}{[(\omega+i\eta)^2 - \epsilon_+^2(\mathbf{k})][(\omega+i\eta)^2 - \epsilon_+^2(\mathbf{k}+\mathbf{q})]}\right\} = 0. \qquad (9)
\end{aligned}$$

The last equality is achieved by shifting the origin to (q_x, q_y), changing the integrated variables $\mathbf{k}$ to $-\mathbf{k}$ and taking the advantage that $\epsilon_+(\mathbf{k}) = \epsilon_+(-\mathbf{k})$. Similar derivations hold for the impurity moment along x and y directions. If the second-order term $\mathcal{O}(V^2)$ is included in the T matrix, the cancellation becomes no longer valid and there is indeed small but finite charge LDOS pattern in the system. In Fig. 7, we plot the numerical results of $\delta\rho(\mathbf{q},\omega)$ at $\omega = 0.05$ and 0.3. It is clear that the amplitude of charge-density variation by magnetic impurities in Fig. 7 is two orders of magnitude smaller than that shown in Fig. 5 by nonmagnetic impurities.

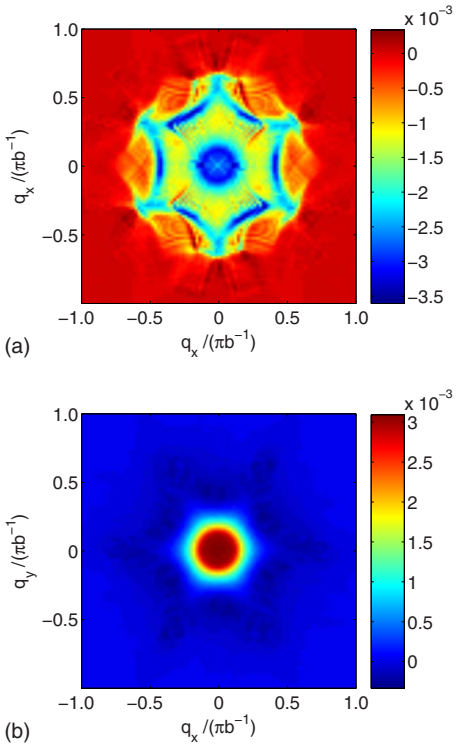

FIG. 7. (Color online) The real part of the Fourier transform of charge local density of states in the case of single magnetic point impurity with its spin polarized along the z axis at (a) $\omega = 0.3$ eV and (b) $\omega = 0.05$ eV.

Therefore, for the magnetic impurity case, we should choose a time-reversal breaking observable to study the interference and a natural choice is the spin local density of states (SLDOS), defined by

$$\vec{S}(\mathbf{r},\omega) = -\frac{1}{\pi}\mathrm{Im}\left[\int dt\,\theta(t)\langle c_\alpha(\mathbf{r},t)\vec{\sigma}^{\alpha\beta}c_\beta^\dagger(\mathbf{r},0)\rangle e^{i\omega t}\right], \qquad (10)$$

where $c_\alpha^\dagger(\mathbf{r},t)$ creates an electron with spin polarization α at position $\mathbf{r}$ and time t. From now on we will only focus on the FT of the z-component SLDOS.

In the case of nonmagnetic impurity, we have demonstrated the absence of interference between $|\mathbf{k},\uparrow\rangle$ and $|-\mathbf{k},\downarrow\rangle$, which form a time-reversal pair. Physically, a time-reversal breaker such as a magnetic impurity can lift this ban on the backscattering. Similar to Eq. (8), it is easy to show that $\langle -\mathbf{k},\downarrow|\hat{V}|\mathbf{k},\uparrow\rangle \neq 0$ due to $\mathcal{T}\sigma_i\mathcal{T}^{-1} = -\sigma_i$. This feature is universal in all of our figures for magnetic impurity. Taking Fig. 8(a) as an example, we can compare it with Fig. 5(a) and notice that although they have common features, the points in the FT-SLDOS that associate with the $2\mathbf{k}_F$ backscattering scattering vectors is only present $(\pm\mathbf{q}_{14}, \pm\mathbf{q}_{25}, \pm\mathbf{q}_{36})$ (see Fig. 4) in the magnetic scattering. We can also compare Fig. 8(b) for magnetic scattering with Fig. 5(b) for nonmagnetic scattering when $\omega = 0.05$ eV. In the latter case, the interference strength universally decays quickly after reaching the boundary of the circle; while in the former case, the interference strength reaches a negative peak across the boundary,

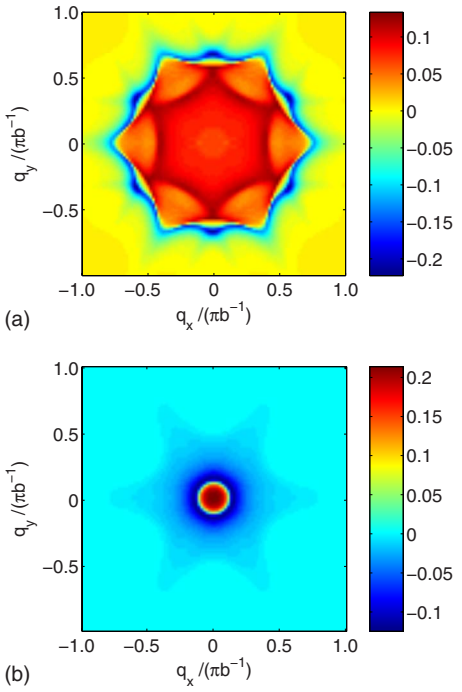

FIG. 8. (Color online) The real part of the Fourier transform of spin local density of states in the case of single magnetic point impurity with its spin polarized along the z axis at (a) $\omega=0.3$ eV and (b) $\omega=0.05$ eV.

indicating a scattering that flips spin moments of the quasiparticles.

Now, we discuss the QPI by magnetic impurities with in-plane magnetic moments. In this case, a unique feature rises in the FT-SLDOS. As shown in Figs. 9 and 10, at $\omega=0.3$ we plot two figures, which correspond to the real and imaginary parts of the FT-SLDOS separately. Similar to the LDOS, the real and imaginary parts correspond to the symmetric and antisymmetric parts of $S_z(x,y,t)$, respectively. For magnetic impurity with magnetic moment along z axis, the symmetric part dominates and the antisymmetric part is either vanishing or orders of magnitude smaller than the symmetric part. However, here as shown in Fig. 9, the antisymmetric part is about three times larger than the symmetric part. The result can be understood as follows. An inversion transformation in a two-dimensional plane, i.e., $(x,y)\rightarrow(-x,-y)$ takes $\hat{\sigma}_z(x,y,t)\rightarrow\hat{\sigma}_z(-x,-y,t)$ and $\hat{\sigma}_{x,y}(-x,-y,t)\rightarrow-\hat{\sigma}_{x,y}(-x,-y,t)$. Therefore, under this transformation, the Hamiltonian without the warping term in the presence of magnetic impurities with in-plane magnetic moments transforms as $H(V_0)\rightarrow H(-V_0)$, where V_0 is the coupling strength of magnetic impurity. Thus, from this symmetry, if we consider $S_z(x,y,t)$ as function of V_0 as well, we have $S_z(x,y,t,V_0)=S_z(-x,-y,t,-V_0)$. Therefore, the first-order correction from the scattering potential vanishes for the symmetry part. In the presence of the warping term, there is no such an exact-symmetry argument. Nevertheless, the symmetric part is still much smaller than the antisymmetric part. In the following, we will first focus on the antisymmetric part.

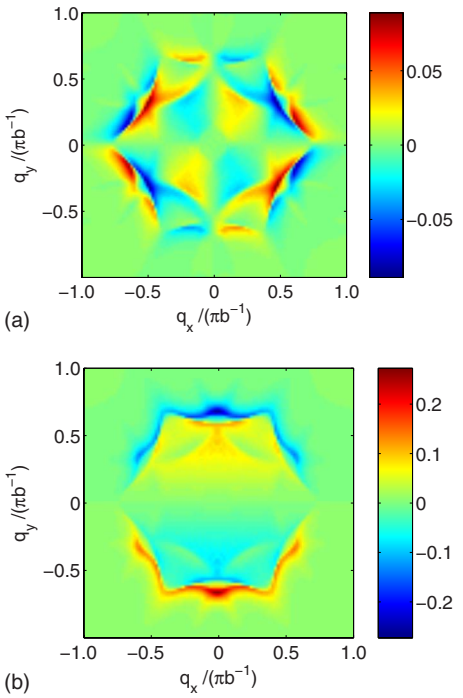

FIG. 9. (Color online) The (a) real part and the (b) imaginary part of the Fourier transform of spin local density of states in the case of single magnetic point impurity with its spin polarized along the y axis at $\omega=0.3$ eV.

Figure 9(b) shows the (antisymmetric) FT-interference pattern for the impurity moment along the y axis at $\omega=0.3$ eV. We find that the strongest interference appears at

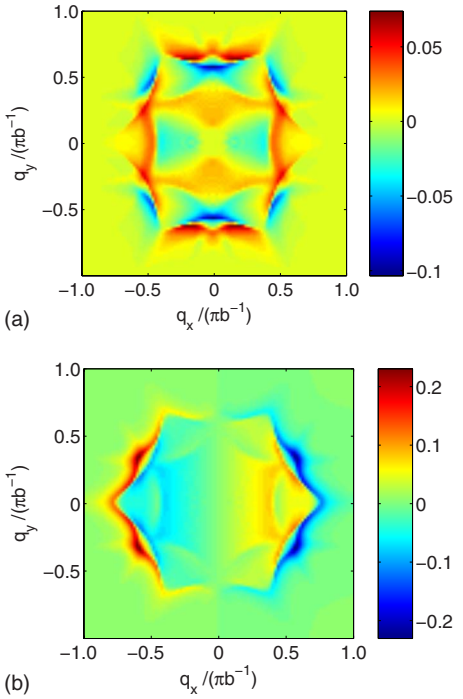

FIG. 10. (Color online) The (a) real part and the (b) imaginary part of the Fourier transform of spin local density of states in the case of single magnetic point impurity with its spin polarized along the x axis at $\omega=0.3$ eV.

wave vector $\pm\mathbf{q}_{51}$ in Fig. 9(b) (q_{ij} is defined in Fig. 4). Moreover, $\mathbf{q}_{13}$ and $\mathbf{q}_{35}$ do not present as strong peaks, in contrast with the cases of the nonmagnetic impurity and the magnetic impurity spin along z axis. In addition, a remarkable feature in the interference pattern is that $S_z^A(\mathbf{q},\omega)$ is zero on the line $q_y=0$. This is caused by an exact symmetry of the system which dictates $S_z(x,y,t)=-S_z(x,-y,t)$. This point will be discussed later in length. Figure 10(b) shows the (antisymmetric) FT-interference pattern for the impurity spin along the x axis at $\omega=0.3$ eV. We can see that the strongest interference is associated with the vertex-to-vertex wave vectors $\mathbf{q}_{13}$ and $\mathbf{q}_{35}$. The strong peak at $\mathbf{q}_{51}$ does not appear and we have $S_z^A(0,q_y,\omega)$ vanishing. This result stems from an approximate equality $S_z(x,y,t)\approx S_z(x,-y,t)$, a point of which will be discussed next.

We can understand above detailed features in the SLDOS from the symmetry analysis of the model. The model obviously has the time-reversal symmetry and the threefold rotation symmetry. Moreover, the model also preserves the $y\rightarrow -y$ mirror symmetry (m_y) but breaks the $x\rightarrow -x$ mirror symmetry (m_x), as can be seen in the warping term. Explicitly, the m_x operator takes $k_\pm$ to $k_\mp$ and σ_z to $-\sigma_z$, which changes the sign of the warping term. Now, let us consider the system in the presence of a magnetic impurity with its spin along y axis. Since $s_y\rightarrow s_y$ under m_y, the whole system still preserves the mirror symmetry m_y. This symmetry directly leads to

$$S_z(x,y,\omega)=-S_z(x,-y,\omega). \tag{11}$$

This symmetry property is clearly demonstrated in Figs. 9(a) and 9(b). On the other hand, if the impurity spin is fixed along the x direction, the system does not have m_x symmetry and we have $S_z(x,y,\omega)\neq -S_z(-x,y,\omega)$. This feature is also demonstrated in Fig. 10(a). If we had $S_z(x,y,\omega)=-S_z(-x,y,\omega)$, we should have $S_z^{A(S)}(q_x,q_y,\omega)=-S_z^{A(S)}(-q_x,q_y,\omega)$ or $S_z(x,y,\omega=S_z(-x,y,\omega)=0$. However, in Fig. 10(a), it is clear that $S_z^S(q_x,q_y,\omega)=S_z^S(-q_x,q_y,\omega)\neq 0$.

The above symmetry is a very important property of the model. In fact, to simply account for the shape of FS, we may also artificially make the Fermi velocity strongly angle dependent while keeping the same spin texture where all spins on the FS are in-plane without tilting. For instance, we can write

$$\tilde{H}(\mathbf{k})=v(\mathbf{k})(k_x\sigma_y-k_y\sigma_x)+\frac{k^2}{2m^*}, \tag{12}$$

where $v(\mathbf{k})=\sqrt{v^2+\lambda^2k^4\sin^2(3\theta)}$ with θ being the azimuthal angle with respect to x axis (ΓM). This model (the in-plane model) has the same dispersion as the model in Eq. (1) but has only in-plane spin texture. The symmetries of the SLDOS here can help us distinguish these two models. For example, one can check these two equations experimentally: $S_z(x,y,\omega)=-S_z(x,-y,\omega)$ for impurity spin polarized along y axis and $S_z(x,y,\omega)=-S_z(-x,y,\omega)$ for impurity spin polarized along x axis. If both are held then the in-plane model suffices but if only one is held, we may need an out-of-plane spin (warping) term. In Table I, we list the property of SLDOS in the two models, Eqs. (1) and (12), in the presence of different types of impurities and under basic symmetry operations.

TABLE I. The symmetry of $S_z(x,y,t)$ under symmetry operations of mirror-x (m_x), mirror-y (m_y), and threefold rotation about z axis (C_3) with impurity spin along three axes. (a) is for the model in Eq. (1) and (b) the model in Eq. (12). "1" means symmetric; "−1" means antisymmetric and "×" means neither of the above. "≈" means it is symmetric (antisymmetric) in the weak impurity strength approximation.

S_z	m_x	m_y	C_3
	(a)		
s_x	×	≈1	×
s_y	×	−1	×
s_z	≈1	≈1	1
	(b)		
s_x	−1	≈1	×
s_y	≈1	−1	×
s_z	≈1	≈1	1

C. Nonmagnetic edge impurity

Step atomic roughness on a surface may be locally idealized into an edge impurity, that is, an infinite line with different but uniform potential on two sides. An edge impurity in a 2D conventional Fermi gas is known to give rise to Friedel oscillation *at fixed energy* in the LDOS. This oscillation can simply be understood as an interference pattern between the incoming plane wave and the reflected wave by the 1D edge. The major contribution comes from the two opposite $\mathbf{k}$ points on the constant-energy contour, $\pm\mathbf{k}_F$ and the oscillation has the wave number $2|\mathbf{k}_F|$ while decaying as a form $1/\sqrt{d}$ where d is the distance from the edge impurity.[22] The same picture is no longer valid if the state at $\mathbf{k}$ and $-\mathbf{k}$ do not scatter with each other, a case for the surface states of a 3D topological insulator where the backscattering is forbidden by the time-reversal symmetry. Therefore the oscillation is expected to decay much faster and thus practically absent in an scanning tunnel microscope (STM) experiment. The "absence" of the Friedel oscillation is considered as a sign of (spin) helical Dirac Fermion systems. However, the oscillation has been observed in STM experiments.[16] The apparent discrepancy between theory and experiment was soon claimed to be superficial and explained by the hexagram shape of the FS.[19] In Sec. III C an exact calculation is performed to test this physical picture.

We consider that the edge impurity is fixed along y axis and the system has zero potential for $x<0$ and uniform potential V for $x>0$. A general quantum state on the left-hand side (LHS) takes the form

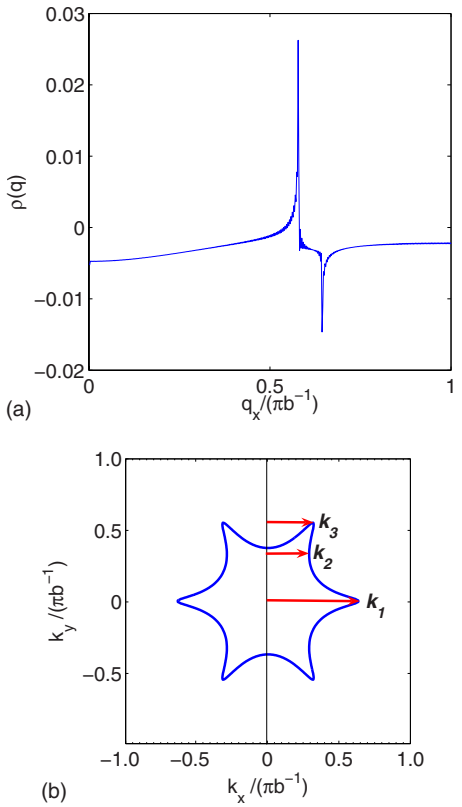

FIG. 11. (Color online) (a) The Fourier transform of the edge-impurity ($V=-0.1$) interference pattern. (b) The three $\mathbf{k}$'s that dominate the interference pattern on the energy contour at $\omega=0.5$ eV.

$$\psi(k_x,k_y;x,y) = \frac{\phi_0(k_x,k_y;x,y) + r\phi_0(-k_x,k_y;x,y)}{\sqrt{1+|r|^2}} \tag{13}$$

and the LDOS is

$$\rho(x,\omega) = \int_{k_x>0} \frac{d^2k}{(2\pi)^2} |\psi(k_x,k_y;x,y)|^2 \delta[\omega - \epsilon_+(k_x,k_y)]. \tag{14}$$

The reflection amplitude r can be obtained together with the transmission amplitude t by matching the boundary condition at the edge, namely,

$$\phi_0(k_x,k_y;0,y) + r\phi_0(-k_x,k_y;0,y) = t\phi_0(k_x'',k_y;0,y), \tag{15}$$

where k_x'' is fixed by the energy conservation $\epsilon(k_x,k_y) = \epsilon(k_x'',k_y) - V$.

Figure 11(a) shows the FT-LDOS for the LHS of the edge impurity at $\omega=0.5$. We can clearly identify the two peaks in the interference associated with $q_x=2\mathbf{k}_2$ and $q_x=2\mathbf{k}_3$, defined in Fig. 11(b). No feature is present at $q_x=2\mathbf{k}_1$, reflecting the absence of backscattering. The spatial dependence of the oscillation, a real-space LDOS, is given in Fig. 12(a). A clear beating pattern can be seen with spatial period $\sim(\mathbf{k}_3-\mathbf{k}_2)^{-1}$. The oscillation decays like $1/|x|^{\alpha}$ where $\alpha\sim0.46$, qualitatively matching the theoretical prediction in the large $|x|$

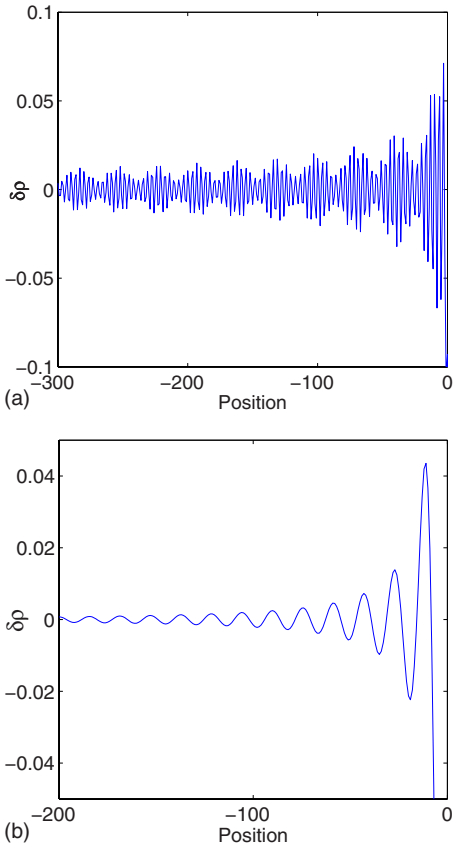

FIG. 12. (Color online) The real-space interference pattern for the edge impurity ($V=-0.1$) at (a) $\omega=0.5$ eV and (b) $\omega=0.05$ eV. The density fluctuation $\delta\rho$ is defined as $\delta\rho=\rho-\rho_0=\rho-1$. The position x is in units of b.

limit.[22,23] When $|x|$ is large enough, the stationary points approximation tells us that, if the edge impurity is along the y axis, the interference pattern is dominated by the $\mathbf{k}$ points where k_x reaches local minimum or maximum. In our model, $\mathbf{k}_{2(3)}$ are the points corresponding to the minimum (maximum) of k_x on the contour of constant energy. However, The existence of such extrema depends on ω. If ω is small enough, the extrema $\mathbf{k}_{2,3}$ disappear and we are left with only $\mathbf{k}_1$. Since $\mathbf{k}_1$ is not allowed to scatter with its time-reversal partner, the decaying of Friedel oscillation becomes $|x|^{-3/2}$ at large $|x|$ [see Fig. 12(b)]. Therefore, there is no universal function for the oscillation decay. The decay depends on the values of parameters. There are two inherent length scales in the model: $b=\sqrt{\lambda/v}$ and $b'=v/\omega$. If $b>1.48b'$, the energy contour is a hexagram and an $1/\sqrt{|x|}$ decay of the oscillation appears while if $b\ll b'$, we have a nearly circular FS and the decay of oscillation takes the form $\rho(x)\sim|x|^{-3/2}$. In the intermediate range, the oscillation varies. For example, at $b=1.2b'$ ($\omega=0.3$), the oscillation decays exponentially for $|x|<100b$ but close to $|x|^{-3/2}$ for $|x|>200b$.

IV. DISCUSSION AND CONCLUSION

The model we have solved produces interference patterns that have enough features to be associated with the topology-protected surface states and the effects of the hexagonal

warping term in 3D topological insulators. However, in order to be more careful before making conclusions, there are two more remarks we would like to mention here.

(i) In our calculations, we neglected the possibility of any ordering due to interaction-induced FS instability. This is valid as long as there is no significant FS nesting vector.[19] In addition, we do not expect strong electron-electron interaction based on the following observation. In experiments on topological insulators, the Fermi level of the sample in general is closer to the bottom of the conduction band and is far away from the Dirac point. Such a system with finite density of states may provide enough screening effect to Coulomb interaction between surface electrons. Moreover, attempting to tune the Fermi level lower by a metallic gate may also lead to the same phenomenon, turning interaction between electrons into irrelevant regime.

(ii) In real systems, there is no "purely magnetic" impurity. A magnetic impurity should also have a nonmagnetic component. This fact does not change our results obtained for magnetic impurities. In the parameter region we choose, the weak impurity approximation is always valid (see a detailed discussion of this approximation in the Appendix A), the nonmagnetic impurity only leads to the charge-density modulation and has little effect on the SLDOS. Namely, the magnetic part of impurity is solely responsible for the SLDOS.

(iii) As we noticed in Sec. III A, the STM experiment done by Zhang *et al.*[15] on [111] surface of Bi_2Te_3 exhibited six peaks in FT-LDOS for the case of nonmagnetic impurities. The experimental result differs from our results shown in Fig. 5(a) by a 30° of rotation. However, this discrepancy can be understood by noticing that in the energy range where they observed the clear interference patterns (50–400 meV), the surface density of states are mixed with bulk states along ΓM. Consequently, due to the superposition of waves with various wavelengths the interference patterns are simply smeared out in these regions. Instead of a full FS we considered here, the dominant interference patterns are then from other unmixed parts of the FS, i.e., the parts along ΓK.

(iv) In an STM experiment done by Alpichshev *et al.*,[16] the decaying behavior of the Friedel oscillation was claimed to be $1/|x|$. However, in the case of 1D edge impurities, our calculation shows $1/|x|^{1/2}$ behavior if the FS shape is dominated by the warping term and $|x|^{-3/2}$ if the warping term is negligible. We believe there are two possible sources of the discrepancy. First, we notice that a simple fitting to the first several periods of oscillation is not enough to determine the decaying behavior. In Fig. 13, we show that the data in Ref. 16 can also be well fitted using an exponentially decaying function as opposed to the $1/|x|$-type fit used in Ref. 16. Second, the experimental measurements are not a pure surface effect. There are bulk electrons in the nearby conduction band which can cause different decaying behavior and complicate the issue. More future experimental measurements are necessary to resolve the issue and test the theoretical predictions.

(v) We also notice that a similar theoretical work[24] focusing solely on nonmagnetic impurity was posted online recently, which suggests the peaks at fixed $\mathbf{q}$'s that correspond to the scattering vectors connecting between second neighbor of the convex parts, and between the nearest neighbor of the vertices of the FS dominate in the QPI patterns. Their results are consistent with our calculations since their results, according to the energy unit in our paper, are obtained at $\omega=0.375$ eV. However, our results suggest that the relative strength between the interference at $\mathbf{q}$'s connecting next-nearest-neighboring vertices (e.g., $\mathbf{q}_{35}$) and the interference at $\mathbf{q}$'s connecting next-nearest-neighboring arc centers (e.g., $\mathbf{q}_{2'4'}$) in the QPI patterns is quite subtle and depends on energy. Therefore, a full T-matrix calculation is necessary in calculating the QPI patterns.

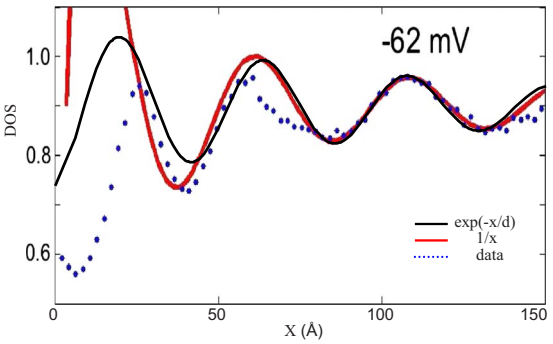

FIG. 13. (Color online) Fitting the experimental data of Ref. 16 using different oscillating functions. The experimental energy −62 meV corresponds to ~0.25 eV in our units. In the exponential fit, $d=107$ Å.

In conclusion, we have investigated the quasiparticle scattering in a 2D helical liquid in the presence of nonmagnetic/magnetic point impurity or a nonmagnetic edge impurity. The inclusion of the hexagonal warping term in our system not only inherits the nature of the k-linear helical liquid but also sharpens our features mentioned above by distorting the shape of the FS. More importantly, it requires an out-of-plane spin texture and can be distinguished from other systems with examination of the mirror symmetries when the magnetic point impurity with in-plane spin moment is present. The absence (presence) of spots in FT-LDOS (FT-SLDOS), corresponding to the backscattering interference, are the essential features to confirm the topological nature of the helical liquid. The results in our work, as may be detected by STM experiments, can be a useful quantum signature, which is uniquely associated with this phase of matter, a 3D topological insulator.

ACKNOWLEDGMENTS

The authors thank Liang Fu for his insights and stimulating discussion and H. Yao for useful conversation.

APPENDIX A: THE WEAK IMPURITY STRENGTH APPROXIMATION

For the parameter we used throughout the paper, the scattering strength is relatively small (i.e., $V_0\rho(\omega)\ll 1$). In this limit the approximation $T(\omega)\approx\hat{V}$ is considerably accurate

(less than 3% error in our case) and many approximate equalities may be derived thereof. This appendix is devoted to explicitly deriving these relations.

First we prove that for a purely magnetic impurity, the induced (charge) LDOS is almost zero everywhere. We prove this by showing $\mathrm{Tr}[\delta G(\mathbf{q},\omega)]\approx 0$. Within the approximation, we have

$$\mathrm{Tr}[\delta G(\mathbf{q},\omega)] \approx \int \frac{d^2k}{4\pi^2}\mathrm{Tr}[G_0(\mathbf{k},\omega)\hat{V}G_0(\mathbf{k}+\mathbf{q},\omega)] = V_0\int \frac{d^2k}{4\pi^2}\mathrm{Tr}[G_0(\mathbf{k},\omega)\sigma_i G_0(\mathbf{k}+\mathbf{q},\omega)]. \tag{A1}$$

In the equation above we do not specify the spin polarization of the impurity and the result is general. Noticing that the system is invariant under time-reversal operation ($C=i\sigma_y$), i.e., $CH(\mathbf{k})C^{-1}=H^T(-\mathbf{k})$ and that a magnetic impurity changes sign under the same operation, i.e., $C\sigma_i C^{-1}=-\sigma_i^T$, we have

$$\begin{aligned}&\int \frac{d^2k}{4\pi^2}\mathrm{Tr}[G_0(\mathbf{k},\omega)\sigma_i G_0(\mathbf{k}+\mathbf{q},\omega)]\\ &= \frac{d^2k}{4\pi^2}\mathrm{Tr}[CG_0(\mathbf{k},\omega)\sigma_i G_0(\mathbf{k}+bq,\omega)C^{-1}]\\ &= -\int \frac{d^2k}{4\pi^2}\mathrm{Tr}[G_0^T(-\mathbf{k},\omega)\sigma_i^T G_0^T(-\mathbf{k}-\mathbf{q},\omega)]\\ &= -\int \frac{d^2k}{4\pi^2}\mathrm{Tr}[G_0(-\mathbf{k}-\mathbf{q},\omega)\sigma_i G_0(-\mathbf{k},\omega)] = 0.\end{aligned} \tag{A2}$$

The last equality may be understood after changing variables $\mathbf{k}\to -\mathbf{k}-\mathbf{q}$.

Next we show that the approximate symmetries listed in part (a) of Table I hold within the same approximation. According to the table, we have, for impurity spin (again it is a purely magnetic impurity) along the z axis, the SLDOS $S_z(x,y,t)\approx S_z(-x,y,t)$, which is equivalent to $S_z(q_x,q_y,\omega)\approx S_z(-q_x,q_y,\omega)$. This may be derived in the following way:

$$\begin{aligned}S_z(\mathbf{q},\omega) &= \mathrm{Tr}[\delta G(\mathbf{q},\omega)\sigma_z] \approx \int \frac{d^2k}{(2\pi)^2}\mathrm{Tr}[G_0(\mathbf{k},\omega)\hat{V}G_0(\mathbf{k}+\mathbf{q},\omega)\sigma_z]\\ &= V\int \frac{d^2k}{(2\pi)^2}\frac{\mathrm{Tr}\left[\left[\omega\sigma_0 - k_y\sigma_x + k_x\sigma_y + \frac{\lambda}{2}(k_+^3+k_-^3)\sigma_z\right]\sigma_z\left\{\omega\sigma_0 - (k_y+q_y)\sigma_x + (k_x+q_x)\sigma_y + \frac{\lambda}{2}[(k+q)_+^3+(k+q)_-^3]\sigma_z\right\}\right]}{[(\omega+i\eta)^2-\epsilon_+^2(\mathbf{k})][(\omega+i\eta)^2-\epsilon_+^2(\mathbf{k}+\mathbf{q})]}\\ &= V\int \frac{d^2k}{(2\pi)^2}\left\{2\frac{\omega^2 + k_y(k_y+q_y) + k_x(k_x+q_x) + \frac{\lambda^2}{4}(k_+^3+k_-^3)[(k+q)_+^3+(k-q)_-^3]}{[(\omega+i\eta)^2-\epsilon_+^2(\mathbf{k})][(\omega+i\eta)^2-\epsilon_+^2(\mathbf{k}+\mathbf{q})]}\right\} \approx S_z(-q_x,q_y,\omega).\end{aligned} \tag{A3}$$

In deriving the last equality, we notice that $\epsilon(k_x,k_y)=\epsilon(-k_x,k_y)$ and change variables as $k_x\to -k_x$. In the second column of part (a) of Table I, we find $S_z(x,y,t)\approx S_z(x,-y,t)$ for the impurity spin in x and z directions. Since $\sigma_y H(k_x,k_y)\sigma_y = H(k_x,-k_y)$, we have

$$\begin{aligned}&S_z(q_x,q_y,\omega)\\ &\approx \int \frac{d^2k}{4\pi^2}\mathrm{Tr}[G_0(k_x,k_y,\omega)\sigma_{x,z}G_0(k_x+q_x,k_y+q_y,\omega)\sigma_z]\\ &= \int \frac{d^2k}{4\pi^2}\mathrm{Tr}[G_0(k_x,-k_y,\omega)(-\sigma_{x,z})\\ &\quad\times G_0(k_x+q_x,-k_y-q_y,\omega)(-\sigma_z)]\\ &= \int \frac{d^2k}{4\pi^2}\mathrm{Tr}[G_0(k_x,k_y,\omega)\sigma_{x,z}G_0(k_x+q_x,k_y-q_y,\omega)\sigma_z]\\ &= S_z(q_x,-q_y,\omega).\end{aligned} \tag{A4}$$

A simple consequence of the weak impurity approximation is a linear combination of LDOS or SLDOS when there is more than one impurity, or an impurity that has both magnetic and nonmagnetic parts. In the latter case, one can simply add up the FT-LDOS and FT-SLDOS for each part to obtain the total configuration. But as discussed in the text, the magnetic part contributes very little to the LDOS and the nonmagnetic part does not contribute to the SLDOS (obvious from time-reversal symmetry), most of the results for the magnetic impurity part remain the same.

APPENDIX B: FRIEDEL OSCILLATION AT FIXED ENERGY IN A 2D DIRAC METAL BY AN EDGE IMPURITY

In the text, we stated that when the energy lies within the "Dirac regime" (e.g., when $\omega=0.05$ eV), the decay of the Friedel oscillation takes the form $\rho(x,\omega)\propto|x|^{-3/2}$. In this appendix the asymptotic expression for the LDOS oscillation caused by an edge impurity in a 2D Dirac metal is derived. The Hamiltonian takes the form

$$H(\mathbf{k}) = v\mathbf{k}\cdot\sigma. \tag{B1}$$

This form is equivalent to the linear part in Eq. (1) up to a global spin-SU(2) gauge. The Hamiltonian may be easily solved: (only positive-energy solutions are listed)

$$\epsilon(\mathbf{k}) = vk,$$

$$\psi(\mathbf{k}) = (e^{i\phi/2}, e^{-i\phi/2})^T/\sqrt{2}, \tag{B2}$$

where ϕ being the polar angle. Now let us suppose that the space is divided in half at $x=0$ (i.e., the edge impurity is along y axis) and the right side has a uniform potential of $V=-V_0$ where $V_0>0$. The continuity of the wave function at $x=0$ gives

$$\begin{pmatrix} e^{i\phi/2} \\ e^{-i\phi/2} \end{pmatrix} + r(\phi)\begin{pmatrix} e^{i\phi'/2} \\ e^{-i\phi'/2} \end{pmatrix} = t(\phi)\begin{pmatrix} e^{i\phi''/2} \\ e^{-i\phi''/2} \end{pmatrix}. \tag{B3}$$

For the refraction part, ϕ'' is fixed by

$$\frac{vk+V_0}{v}\sin(\phi'') = k\sin(\phi). \tag{B4}$$

And for the reflection part, $\phi' = \pi - \phi$. Solving these equations, one has

$$r = -\frac{\sin\left(\frac{\phi-\phi''}{2}\right)}{\cos\left(\frac{\phi+\phi''}{2}\right)},$$

$$t = \frac{\cos(\phi)}{\cos\left(\frac{\phi+\phi''}{2}\right)}. \tag{B5}$$

Using the stationary phase approximation, we know that after integrating all the $\mathbf{k}$'s on the fixed energy contour $\omega = vk$ to obtain the LDOS, the contribution mainly comes from the $\mathbf{k}$'s that have small polar angles. At small angles, the reflection index takes the form

$$r(\phi) \approx -\frac{V_0}{2(V_0+vk)}\phi. \tag{B6}$$

Using Eq. (14), we have

$$\begin{aligned}\rho(x,\omega) &\approx \int_{-\pi/2}^{\pi/2}\frac{d\phi}{2\pi}\frac{V_0}{V_0+\omega}\phi^2\sin\left(\frac{2\omega}{v}\cos(\phi)x\right) \\ &\approx \int_{-\infty}^{\infty}\frac{d\phi}{2\pi}\frac{V_0}{V_0+\omega}\mathrm{Im}[\phi^2 e^{i2\omega/v\cos(\phi)x}] \\ &\approx \frac{V_0}{V_0+\omega}\frac{\sqrt{\pi}}{4}\cos\left(\frac{2\omega}{v}x-\frac{\pi}{4}\right)\left(\frac{2\omega}{v}x\right)^{-3/2}.\end{aligned} \tag{B7}$$

[1] Liang Fu, C. L. Kane, and E. J. Mele, Phys. Rev. Lett. **98**, 106803 (2007).
[2] X.-L. Qi, T. L. Hughes, and S.-C. Zhang, Phys. Rev. B **78**, 195424 (2008).
[3] H. Zhang, C. X. Liu, X. L. Qi, X. Dai, Z. Fang, and S.-C. Zhang, Nat. Phys. **5**, 438 (2009).
[4] D. Hsieh, D. Qian, L. Wray, Y. Xia, Y. S. Hor, R. J. Cava, and M. Z. Hasan, Nature (London) **452**, 970 (2008).
[5] D. Hsieh, Y. Xia, L. Wray, D. Qian, A. Pal, J. H. Dil, J. Osterwalder, F. Meier, G. Bihlmayer, C. L. Kane, Y. S. Hor, R. J. Cava, and M. Z. Hasan, Science **323**, 919 (2009).
[6] D. Hsieh, Y. Xia, D. Qian, L. Wray, J. H. Dil, F. Meier, J. Osterwalder, L. Patthey, J. G. Checkelsky, N. P. Ong, A. V. Fedorov, H. Lin, A. Bansil, D. Grauer, Y. S. Hor, R. J. Cava, and M. Z. Hasan, Nature (London) **460**, 1101 (2009).
[7] Y. L. Chen, J. G. Analytis, J.-H. Chu, Z. K. Liu, S.-K. Mo, X. L. Qi, H. J. Zhang, D. H. Lu, X. Dai, Z. Fang, S. C. Zhang, I. R. Fisher, Z. Hussain, and Z.-X. Shen, Science **325**, 178 (2009).
[8] Y. Xia, D. Qian, D. Hsieh, L. Wray, A. Pal, H. Lin, A. Bansil, D. Grauer, Y. S. Hor, R. J. Cava, and M. Z. Hasan, Nat. Phys. **5**, 398 (2009).
[9] Y. S. Hor, A. Richardella, P. Roushan, Y. Xia, J. G. Checkelsky, A. Yazdani, M. Z. Hasan, N. P. Ong, and R. J. Cava, Phys. Rev. B **79**, 195208 (2009).
[10] L. Fu and C. L. Kane, Phys. Rev. B **76**, 045302 (2007).
[11] C. Wu, B. A. Bernevig, and S.-C. Zhang, Phys. Rev. Lett. **96**, 106401 (2006).
[12] A. K. Geim and K. S. Novoselov, Nature Mater. **6**, 183 (2007).
[13] H. Peng, K. Lai, D. Kong, S. Meister, Y. Chen, X.-L. Qi, S.-C. Zhang, Z.-X. Shen, and Y. Cui, arXiv:0908.3314 (unpublished).
[14] P. Roushan, J. Seo, C. V. Parker, Y. S. Hor, D. Hsieh, D. Qian, A. Richardella, M. Z. Hasan, R. J. Cava, and Ali Yazdani, Nature (London) **460**, 1106 (2009).
[15] T. Zhang, P. Cheng, X. Chen, J.-F. Jia, X. Ma, K. He, L. Wang, H. Zhang, X. Dai, Z. Fang, X. Xie, and Q.-K. Xue, arXiv:0908.4136 (unpublished).
[16] Z. Alpichshev, J. G. Analytis, J.-H. Chu, I. R. Fisher, Y. L. Chen, Z. X. Shen, A. Fang, and A. Kapitulnik, arXiv:0908.0371 (unpublished).
[17] K. K. Gomes, W. Ko, W. Mar, Y. Chen, Z.-X. Shen, and H. C. Manoharan, arXiv:0909.0921 (unpublished).
[18] J. E. Hoffman, K. McElroy, D.-H. Lee, K. M. Lang, H. Eisaki, S. Uchida, and J. C. Davis, Science **297**, 1148 (2002); K. McElroy, R. W. Simmonds, J. E. Hoffman, D.-H. Lee, J. Orenstein, H. Eisaki, S. Uchida, and J. C. Davis, Nature (London) **422**, 592 (2003).
[19] Liang Fu, arXiv:0908.1418 (unpublished).
[20] For instance, D. K. Morr and N. A. Stavropoulos, Phys. Rev. B **67**, 020502(R) (2003); Q.-H. Wang and D.-H. Lee, *ibid.* **67**, 020511(R) (2003); C. Bena, S. Chakravarty, J. Hu, and C.

Nayak, *ibid.* **69**, 134517 (2004).

[21] As a complementary and insightful study considering the effect of magnetic impurities, Q. Liu, C.-X. Liu, C. Xu, X.-L. Qi, and S.-C. Zhang, Phys. Rev. Lett. **102**, 156603 (2009), focused on the profound physics near the Dirac point, where $\omega \ll V_{MI}$.

[22] M. F. Crommie, C. P. Lutz, and M. Eigler, Nature (London) **363**, 524 (1993).

[23] Liang Fu, private communication.

[24] W.-C. Lee, C. Wu, D. P. Arovas, and S.-C. Zhang, arXiv:0910.1668 (unpublished).